Environ Fluid Mech (2014) 14:849–871
DOI 10.1007/s10652-013-9329-9

ORIGINAL ARTICLE

Quantifying the effect of wind on internal wave resonance in Lake Villarrica, Chile

Carlos Rozas · **Alberto de la Fuente** ·
Hugo Ulloa · **Peter Davies** · **Yarko Niño**

Received: 10 April 2013 / Accepted: 14 December 2013 / Published online: 25 December 2013

Abstract Lake Villarrica, located in south central Chile, has a maximum depth of 167 m and a maximum fetch of about 20 km. The lake is monomictic, with a seasonal thermocline located at a depth of approximately 20 m. Field data show the presence of basin-scale internal waves that are forced by daily winds and affected by Coriolis acceleration. A modal linear and non-linear analysis of internal waves has been used, assuming a two-layer system. The numerical simulations show good agreement with the internal wave field observations. The obtained modes were used to study the energy dissipation within the system, which is necessary to control the amplitude growth. Field data and numerical simulations identify (1) the occurrence of a horizontal mode 1 Kelvin wave, with a period of about a day that coincides with the frequency of daily winds, suggesting that this mode of the Kelvin waves is in a resonant state (subject to damping and controlled by frictional effects in the field) and (2) the presence of higher-frequency internal waves, which are excited by non-linear interactions between basin-scale internal waves. The non-linear simulation indicates that only 10 % of the dissipation rate of the Kelvin wave is because of bottom friction, while the rest 90 % represents the energy that is radiated from the Kelvin wave to other modes. Also, this study shows that modes with periods between 5 and 8 h are excited by non-linear interactions between the fundamental Kelvin wave and horizontal Poincaré-type waves. A laboratory study of the resonant interaction between a periodic forcing and the internal wave field response has also been performed, confirming the resonance for the horizontal mode 1 Kelvin wave.

Keywords Lake Villarrica · Kelvin wave · Modal analysis · Resonance

C. Rozas (✉) · A. de la Fuente · H. Ulloa
Departamento de Ingeniería Civil, Universidad de Chile, Santiago, Chile
e-mail: crozas@ing.uchile.cl

P. Davies
Department of Civil Engineering, University of Dundee, Dundee, UK

Y. Niño
Departamento de Ingeniería Civil and Advanced Mining Technology Center,
Universidad de Chile, Santiago, Chile

1 Introduction

The interaction between the wind and the internal waves in lakes and reservoirs can be analysed in terms of a forced harmonic oscillator, in which the wind provides energy to the lake, moving the thermocline from its equilibrium position and generating internal waves [22, 34]. When the wind stops, the excited waves propagate around the basin until damping mechanisms, such as bottom and wall friction, dissipate their energy [28,29]. Nevertheless, wind forcing of lakes is typically periodic and so the interaction between the wind and the internal waves can be seen as a forced oscillatory system that admits a resonance response [2,20].

As a harmonic oscillator, resonance arises when the forcing frequency matches the fundamental frequency of the system. Antenucci and Imberger [2] have studied the seasonal evolution of the natural frequencies of Lake Kinneret and identified a resonant interaction between the wind and the dominant radial, azimuthal and vertical mode 1 Kelvin wave, both with periods close to 24 h. According to these authors, when the natural frequency of the Kelvin wave gets closer to the wind frequency (period of 24 h), the amplitude of the internal waves is larger than those observed when the natural frequency of the Kelvin wave moves away from the forcing frequency. Resonance can amplify the response of internal wave modes that are not energized by the surface winds, such as the second vertical mode [23]. Evidence of the resonant interaction is also shown in the experiments performed by Wake et al. [38] for the non-rotating case, in which it is seen that resonance can excite harmonics of the fundamental frequency. In the same sense, non-rotating experiments performed by Boegman and Ivey [3] show that resonance increases the nonlinear steepening of basin-scale internal seiches, enhancing the energy flux to progressive non-linear internal waves [3]. In practical terms, amplitudes of basin-scale internal waves cannot grow unbounded and so damping mechanisms act in order to dissipate the energy that periodically enters to the basin-scale waves. Such mechanisms include wave breaking and shoaling [4,5,9,27], bottom friction [16,26], spin-down and wave-canceling [29,30], diapycnal mixing due to Kelvin-Helmholtz instabilities [3], shear-induced instabilities and critical wave reflection [40].

The aim of this article is to characterize and quantify the resonance between Kelvin wave and the periodic wind. This aim is achieved by studying, first, the clear resonance between the periodic wind and the basin-scale waves that was observed in Lake Villarrica, located in south central Chile The lake is a monomictic temperate lake, with a seasonal thermocline located at about 20 m deep. Field measurements that reveal the resonant interaction are analysed based on a modal analysis [28,31] that allows for quantifying the energy fluxes involved on this phenomenon, focusing on the evolution of internal waves affected by Coriolis acceleration and on their resonant interaction with periodic winds. Second, laboratory experiments were conducted to study in detail the features that characterize the resonant interaction between basin-scale waves and the wind forcing in a rotating table. This paper is structured as follows: (i) the field study, the two-layer definition and the numerical scheme applied are described; (ii), field, numerical and experimental results are presented; (iii) finally, results are discussed in terms of the observed wind-wave resonance and its implications.

2 Methods

2.1 Field study

Lake Villarrica is a monomictic lake located in south central Chile (39.25°S, 72.10°W), with a rectangular-like shape of 20 km × 10 km, oriented along the east-west direction. The

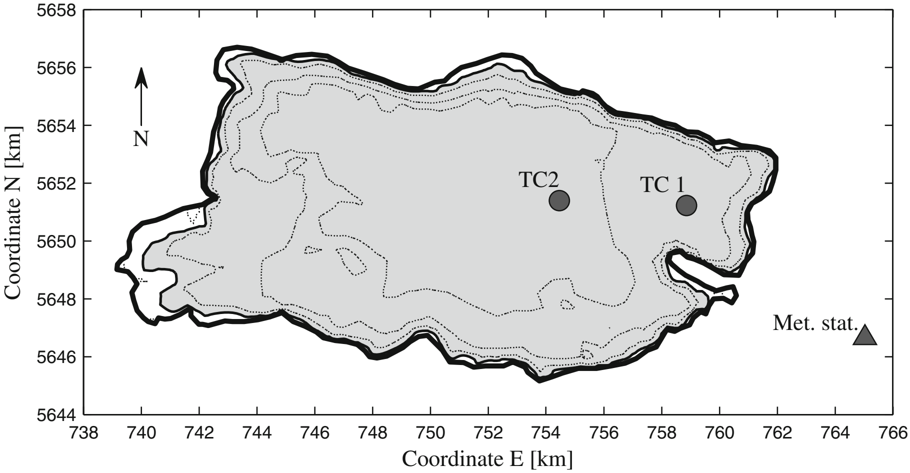

Fig. 1 Lake Villarrica bathymetry and location of thermistor chains (TC1 and TC2) and meteorological station (Met. Stat.). Depth contours every 50 m, and *grey area* denotes the basin interface area located at 18.5 m depth

surface area of the lake is of about 176 km^2, a maximum depth of 167 m and a maximum fetch of about 20 km. The average depth is 120 m and the dimensions of the lake indicate that the Earth's rotation is important for the internal wave dynamics during summer time [19]. Two thermistor chains were deployed in the lake between 8 and 20 February 2009 (days 39–51 of 2009), corresponding to the austral summer time when Lake Villarrica shows a strong thermal stratification. As shown in Fig. 1, one of the thermistor chains (TC1) was located at the east end of the lake and the other at the center of the lake (TC2). Each chain was 80 m long, formed by 17 HOBO underwater temperature loggers sampling every 30 s, vertically distributed with maximum resolution of 2 m in the thermocline region at 20 m depth [19]. Figure 2b, c show water temperature measurements, where horizontal white lines in the right-hand vertical axis indicate location of temperature data loggers. Finally, one meteorological station was installed in the lake vicinity (see Fig. 1) to record wind direction and magnitude, averaged every 10 min. Figure 2a shows measured time series of wind speed and direction. Lake Villarrica is surrounded by mountains in its northern and southern shore, so the wind over the lake blows in the east-west direction as it was recorded in the meteorological station. Then, homogeneous wind over the lake is a reasonable approximation to the problem.

2.2 Two-layers definition

Measurements shown in Fig. 2 indicate that the thermal structure of the lake can be modeled conceptually as a two-layer system, with the corresponding thermocline being located at the depth at which the maximum of the time-averaged vertical profiles of the buoyancy frequency, N, occurs (18.5 m depth, see Fig. 3) [10]. Figure 3 was constructed by the isopycnal averaging [25], where large values of buoyancy frequency near the surface are attributed to diurnal heat exchanges with the atmosphere. Here $N(z) = \sqrt{-g/\rho\,(\partial\rho/\partial z)}$ of Fig. 3b was computed with the vertical density profile of Fig. 3a. In this equation, g is the acceleration due to gravity, ρ is the density and z is the vertical axis pointing upwards. For each thermistor

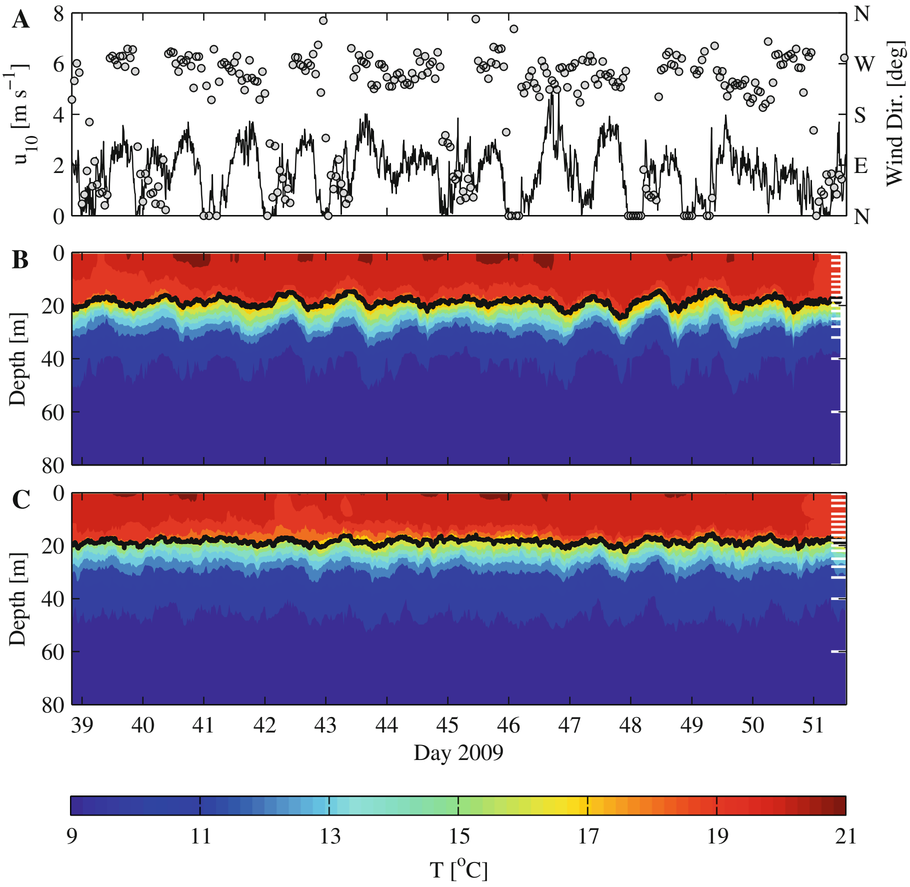

Fig. 2 **a** Wind direction (*dots*) and wind speed (*line*). **b** and **c** temperature distribution at TC1 and TC2, and estimated density interface (*dark line*). *Horizontal white lines* in the right-hand vertical axis indicate location of temperature data loggers

chain, the layer-averaged water densities are summarized in Table 1. The time series of the thermocline displacements, for both thermistor chains, were defined empirically in terms of the isotherm that, in average, is located at a depth of 18.5 m. The time-histories of the thermocline displacements so-defined are shown as thick lines in Fig. 2 for stations TC1 and TC2. The grey area in Fig. 1 indicates the basin density interface area at 18.5 m depth, shown here to cover almost the entire surface area.

2.3 Modal analysis

This section summarizes the general aspects of modal analysis required to understand the methodology used in this article. However, given length restriction of the article, some details are not provided and it is left to the reader to visit the article [31] for the basic concepts on modal analysis, [28] for bulk energy dissipation and bottom friction, and [9] for non-linear interactions among internal waves.

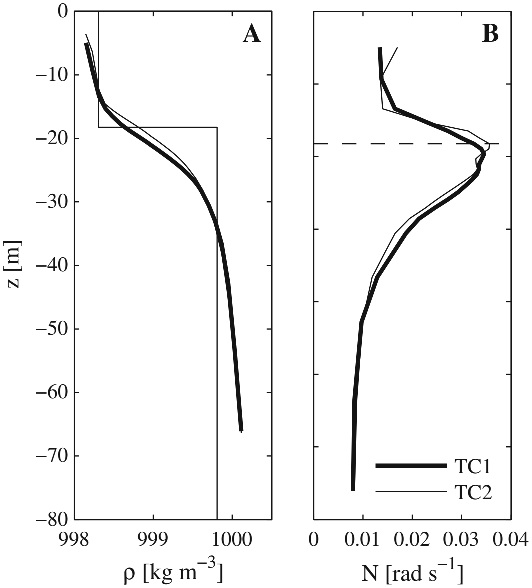

Fig. 3 **a**, **b** Average vertical profiles of density and buoyancy frequency for TC1 and TC2. The *thin line* corresponds to two-layer system average densities and the *dashed line* indicates the location of the thermocline

Table 1 Average water densities of the two-layer model for both thermistor chains and mean values for numerical simulation

Parameter (kg m^{-3})	TC1	TC2	Mean
ρ_1	998.31	998.34	998.331
ρ_2	999.81	999.82	999.82
$\Delta\rho$	1.50	1.48	1.49

2.3.1 General overview

The modal analysis first proposed by Shimizu et al. [31] was followed to simulate the response to the wind of the two-layer stratified system. This pseudo-spectral approach solves the eigenvalue problem that arises from searching for periodic waves solutions to the linearized homogeneous two-layer equations. Then, after assuming that any unknown variable is represented by the linear combination of the basin-scale waves described by the eigenvectors, the problem is reduced to compute the modal amplitudes of that linear combination [31]. Following this methodology, the two-dimensional, two-layer problem is simplified to a set of R ordinary differential equations, each one representing the evolution of each one of the R basin-scale waves. For the linear inviscid case, these equations are written as:

$$\frac{d\tilde{a}_r}{dt} = i\omega_r\tilde{a}_r + \tilde{f}_r \tag{1}$$

where $\tilde{a}_r(t)$ denotes the complex amplitude of the rth basin-scale wave, ω_r the corresponding natural frequency of oscillation (the eigenvalues of the problem), $i = \sqrt{-1}$ is the imaginary unit and $\tilde{f}_r$ is a function that describes the momentum exchanges between each basin-scale wave and the wind field. The energy contained on the rth mode is computed as:

$$E_r = e_r\frac{\tilde{a}_r\tilde{a}_r^*}{2} \tag{2}$$

where e_r is a normalizing factor and superscript * denotes the complex conjugate.

2.3.2 Bulk energy dissipation of the Kelvin wave

Shimizu and Imberger [28] showed that energy dissipation may be included in the modal analysis by introducing bulk linear dissipation rate coefficients, γ_r, thus modifying Eq. 1 as:

$$\frac{d\tilde{a}_r}{dt} = (i\varpi_r - \gamma_r)\ \tilde{a}_r + \tilde{f}_r \tag{3}$$

where ϖ_r is the modal frequency of the rth basin-scale wave (assumed to be slightly different from ω_r because of several factors including friction [28] and nonlinear interactions between waves [9,13]) and γ_r is a real positive constant. Following Shimizu and Imberger [28], non-dissipative modes of the eigenvalue problem can be used for fitting the interface displacements simulated with the modal analysis to the observed values obtained from the thermistor chains. The free parameters of this problem are the energy damping coefficients, γ_r, modal frequencies modified by friction, ϖ_r and initial complex amplitudes $\tilde{a}_{r_o}$. These free parameters were estimated using an optimization process that aims to minimize the difference between time series of the interface displacements observed at each thermistor chain and those computed on the basis of the complex amplitudes. The fitted angular frequency was restricted to the range $0.5\omega_r \leq \varpi_r \leq 1.5\omega_r$, the damping timescales, $T_{dr} = 2\pi\gamma_r^{-1}$ were restricted to be between 1 and 80 days and no restrictions were imposed on the initial complex amplitude.

2.3.3 Nonlinear interaction

Finally, de la Fuente et al. [9] included non-linear interactions among basin-scale waves to the modal analysis, which provides that the complex amplitude of the rth mode is described by:

$$\frac{d\tilde{a}_r}{dt} = (i\omega_r - \gamma_r)\,\tilde{a}_r + i\sum_{s=-\infty}^{+\infty}\sum_{q=-\infty}^{+\infty}\tilde{n}^{(r,q,s)}\tilde{a}_q\tilde{a}_s + \tilde{f}_r \tag{4}$$

where $\tilde{n}^{(r,q,s)}$ is a coefficient that quantifies the magnitude of the changes in the complex amplitudes of the rth mode, due to the non-linear interaction among the rth, qth and sth modes [9]. Contrary to Eq. 3, the energy damping coefficients, γ_r, in Eq. 4 should only account for energy dissipation due to bottom friction. Considering this, the energy damping coefficient were computed following Shimizu and Imberger [28], linearizing the bottom shear stress in such a way that the eigenvalues of the problem are now complex numbers, whose imaginary part are equal to γ_r. The linearization of the bottom shear stress requires writing it as $\boldsymbol{\tau}_b = \rho C'_d\mathbf{u}$, where $C'_d = C_d\tilde{u}$ is the modified bottom drag coefficient, being $C_d = 2–3\,times\,10^{-3}$ the bottom drag coefficient according to [28] and the references therein. $C_d = 2.5\times10^{-3}$ was used here and $\tilde{u}$ is the velocity scale of the lower layer that was obtained based on the inviscid simulation. Finally, $\tilde{f}_r$ and ω_r in Eq. 4 are the same values required for the linear inviscid problem of Eq. 3. Non-linear interactions among basin-scale waves were studied based on preserving the energy cascade feature of the flow [9] so 47 gravitation internal waves were required to simulate the dynamics of the nine largest modes. As a consequence of the energy cascade behaviour the energy is concentrated in the smaller waves, which impose a restriction on the length of the simulation to one week. Opposite to Eq. 3, only the initial complex amplitudes are the free parameters of the problem. This initial condition was estimated by using the linear inviscid equation (Eq. 1), and the optimization process that aims

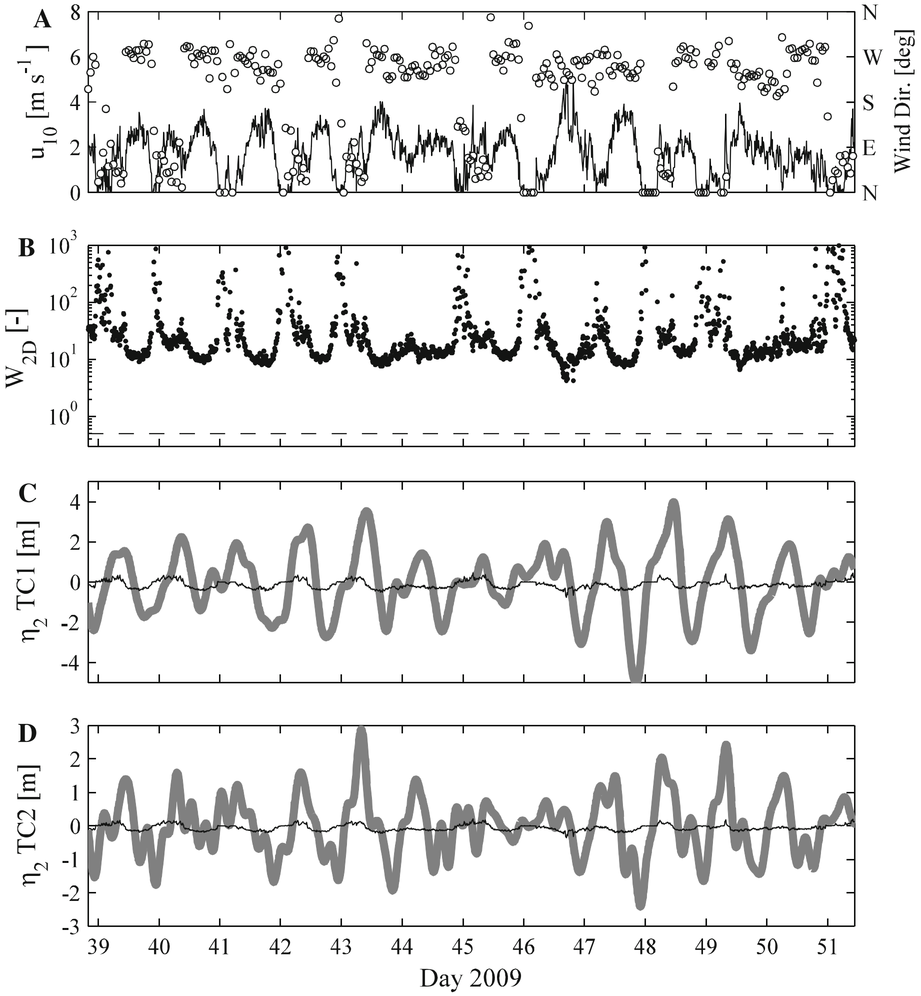

Fig. 4 **a** Wind direction (*dots*) and wind speed (*line*). **b** Wedderburn 2D number for Lake Villarrica. **c**, **d** Observed interface displacements (*thick gray line*) and predicted interface displacements using W2D (*thin line*) at TC1 and TC2.

to minimize the difference between time series of the interface displacements observed at each thermistor chain and those computed on the basis of the linear problem. The first 3 days of measurements were used for fitting the initial amplitude and, given this initial condition, the non-linear problem was directly solved based on Eq. 4.

3 Results

3.1 Field measurements

Figure 4 displays wind data (magnitude and direction), the Wedderburn 2D number, W_{2D} [32] and the vertical displacements of the thermocline observed at TC1 and TC2, filtered with a band-pass filter that cuts terms in the Fourier transform out of the range between

5 h and 3 days. In Fig. 4a it is observed that wind blows with daily frequency from the west and the maximum speed is less than 5 m/s. Furthermore, internal wave activity is evident in the records (Fig. 4c, d), with a larger amplitude observed at TC1 rather than TC2, because TC1 is located near the perimeter of the lake where isotherm displacements are usually large due to the presence of internal Kelvin waves in Coriolis-affected lakes [2,14,39].

Wind is the most important momentum source for the water body dynamics, inducing surface currents and basin-scales internal waves [16]. To explore the order of magnitude of wind-induced isotherm displacements, the Wedderburn 2D number (W_{2D}) for a two-layer stratification was computed following Shintani et al. [32], with the observed wind shear stress. W_{2D} is an extension of the standard Wedderburn number [17,33] for irregular basins with vertical walls as is the case of Lake Villarrica (Fig. 1), and is defined as:

$$W_{2D} = \frac{h_1}{2\eta_{2\,\max}} = \frac{gh_1^2}{2x_g u_*^2} \tag{5}$$

where $\eta_{2\,\max}$ is the maximum interface displacement in the upwind end of the basin interface area, u_* denotes the wind shear velocity, and x_g is the distance between the upwind end and centroid of the basin interface area. Figure 4b shows the time series of W_{2D}, in which small values of W_{2D} imply large interface displacements, with $W_{2D} = 0.5$ being the condition for strong upwelling in the linear case [32]. Assuming a linearly-tilted thermocline, the wind-induced interface displacements, $\eta_2(\vec{x})$, at TC1 and TC2 locations were estimated as:

$$\eta_2(\vec{x}) = \frac{h_1}{W_{2D}} \frac{d(\vec{x})}{x_g} \tag{6}$$

where $d(\vec{x})$ is the distance along the wind direction between the centroid of the basin interface area and the place $(\vec{x})$ where isotherm displacements is being calculated and h_1 is the upper layer height (18.5 m). By using of W_{2D} to estimate the thermocline response to the wind, we were able to define whether the displacements are expected to be either negative or positive, depending on if the thermistor chain is located up- or down-wind the geometric centre of the lake [32]. In the particular case of Lake Villarrica, maximum wind magnitudes are associated to wind blowing from the West (see Fig. 4a), so that thermocline displacements in TC1 are expected to be negative for these winds. Figure 4c, d shows the comparison between observed isotherm displacements and wind-induced interface displacements, estimated with Eq. 6 at TC1 and TC2, respectively. The computed Wedderburn numbers are larger than 20 (Fig. 4b), so the expected interface displacements at the perimeter of the lake are less than about 50 cm (Fig. 4c, d), which has no correlation with the measurements that shows internal wave amplitudes of about 2–3 m. It is important to remind that this analysis only explores the order of magnitude of interface displacements expected for the measured wind shear velocity. Based on this preliminary estimation, it is possible to see that wind shear stress is not strong enough to generate the observed interface amplitudes. The hypothesis discussed in the rest of this article is that this extra energy is provided by resonant interactions between the periodic wind and some of the basin-scale internal waves in the lake.

Strictly speaking, in lakes substantially wider than the Rossby radius of deformation [1], upwelling occurs in the form of Ekman-driven upwelling along the coasts that are parallel to the wind due to Coriolis force [7,12], and not on the upwind end of the lake as assumed in the derivation of Eq. 6. Nevertheless, in this case the Wedderburn 2D number represents

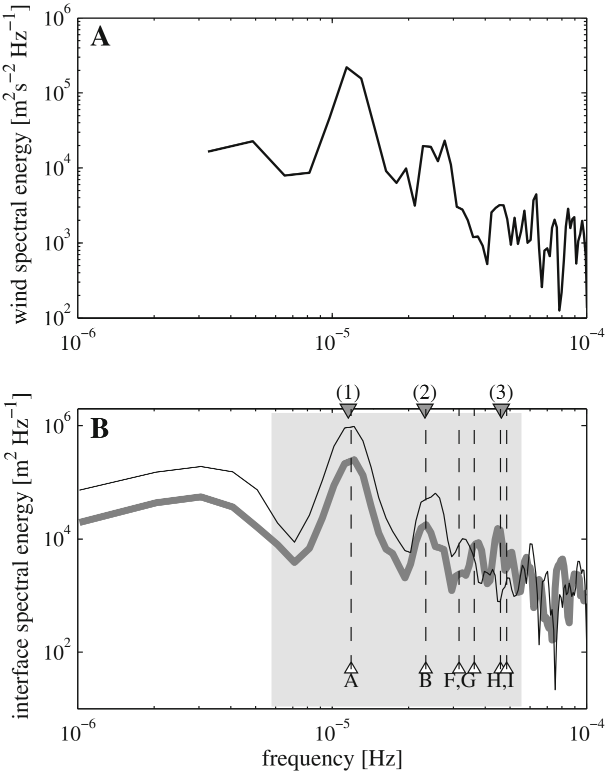

Fig. 5 **a** Power spectral density of wind time series. **b** Power spectral density of the interface displacements at TC1 (*black thin line*) and TC2 (*grey thick line*). Periods in **b** (1) 24 h, (2) 12 h and (3) 6 h. *Letters a–i* refer to the modes shown in Fig. 6

a first approach in order to quantify the order of magnitude of the wind-induced interface displacements, before rotation starts to affect the basin-scale internal waves generated from wind-generated seiches. Winds blowing over Coriolis affected lakes generate Ekman layers and upwelling occurring in the coasts takes the form of internal Kelvin waves in the stratified case [7].

A spectral analysis of time series of the wind speed and interface displacements is shown in Fig. 5a and b, respectively. Figure 5a shows that the dominant periods in the wind time-series are 24 and 12 h, although the energy contained in the 12 h peak is one order of magnitude smaller that the energy contained in the 24 h peak. Furthermore, Fig. 5b demonstrates three dominant periods marked with numbers in the upper horizontal axis, namely: periods (1) and (2) of about 24 and 12 h, respectively, associated with maximum values in both TC1 and TC2, and period (3) of about 6 h, which presents maximum values in the middle of the lake (TC2) rather than in the perimeter (TC1). All of these peaks can be associated with different modes of the internal oscillations (marked by dashed lines in Fig. 5) and are further analysed in the next section using numerical simulations of basin-scale internal waves. The grey area defined in Fig. 5b shows the range of frequencies studied in this article that contains all of the energetic frequencies in both the wind speed and the interface displacement.

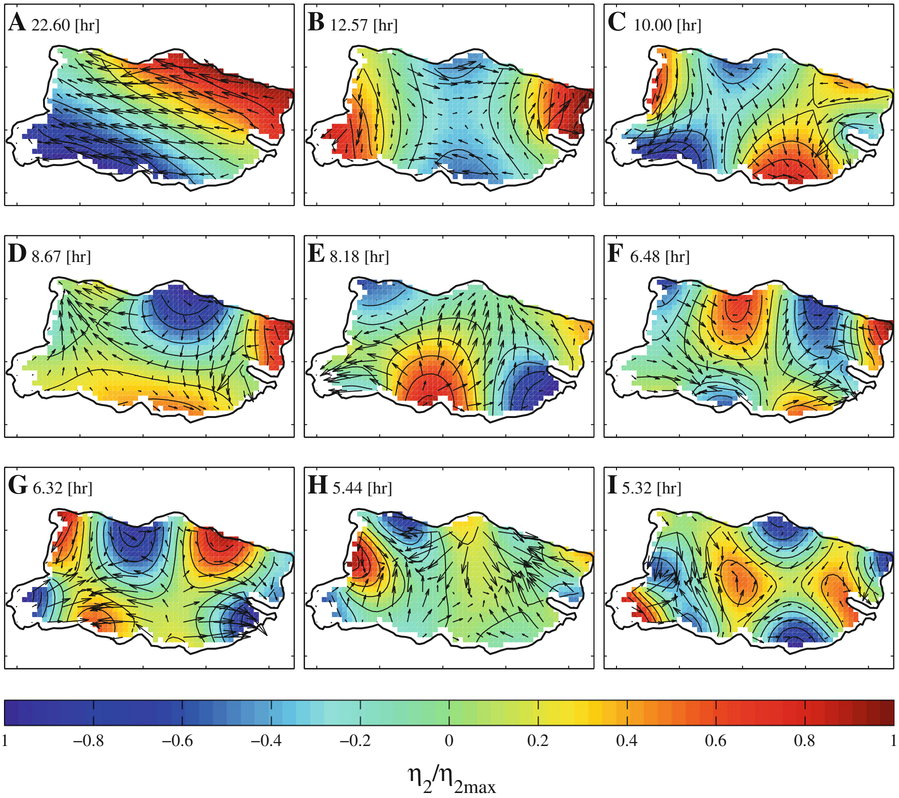

Fig. 6 Spatial shape of nine computed gravitational basin-scale waves of Lake Villarrica

3.2 Basin-scale waves in Lake Villarrica

The numerical solution of the modal analysis was carried out following [31] in a rectangular, staggered mesh of square elements of side 250 m. This computation was conducted with layer thickness $h_1 = 18.5\,\text{m}$, h_2 depending on the bathymetry and $\Delta\rho = 1.49\,\text{kg/m}^3$ (Table 1). Figure 6 shows the horizontal shape of interface displacements and the upper layer flow velocity of the nine largest gravitational internal waves with natural periods larger than 5 h used for this research. These waves were identified as gravitational waves because the potential wave energy is of the same order as the kinetic energy [31]. Further detail is provided in Table 2. The use of these nine internal gravitational waves for the analysis responds to the fact that most of the observed energy in both the wind speed and interface displacements is concentrated in periods larger than 5 h (see grey area of Fig. 5b). The main spectral peak in both thermistor chains has a period of about 1 day and is associated with the fundamental Kelvin wave, whose natural period calculated by the modal analysis is 22.60 h. Figure 6b shows the Kelvin wave horizontal mode (K2) with a natural period of 12.47 h. Moreover, modal analysis also identifies Poincaré-type waves: horizontal mode 3 wave with period of 10.00 h (Fig. 6c), horizontal mode 4 wave with period 6.48 h (Fig. 6f) and two horizontal mode 5 waves with periods of 6.32 and 5.44 h (Fig. 6g and H, respectively). In the context of this article, horizontal mode 4 has four peaks and four valleys in the interface, as shown in Fig. 6. Finally, horizontal modes identified in Fig. 6 rotate according to Coriolis acceleration.

Table 2 Adjusted parameters for fitted modes in the optimization process.

Mode	Panel	Classification	$2\pi\omega_r^{-1}$ (h)	$2\pi\varpi_r^{-1}$ (h)	Difference (%)	$2\pi\gamma_r^{-1*}$ (days)	$2\pi\gamma_r^{-1**}$ (days)
1	a	K1	22.6	23.3	−3.1	30.2	419
2	b	K2	12.5	18.7	−50.0	1.1	309
3	c	P3.1	10.0	10.3	−3.1	80.0	232
4	d	P3.2	8.7	13.0	−50.0	80.0	371
5	e	P4.1	8.2	12.3	−50.0	1.0	244
6	f	P4.2	6.5	7.6	−18.0	80.0	206
7	g	P5.1	6.3	9.1	−44.2	20.1	254
8	h	P5.2	5.4	8.2	−50.0	1.0	145
9	i	P6.1	5.3	8.0	−50.0	1.0	163

Column labeled with $2\pi\omega_r^{-1}$ corresponds to period computed with eigenvalue problem, column $2\pi\varpi_r^{-1}$ shows modified periods based on fitting technique. Column "Difference" indicates percentage of difference between $2\pi\varpi_r^{-1}$ and $2\pi\omega_r^{-1}$. Last two columns show the energy damping timescale ($2\pi\gamma_r^{-1}$) computed with fitting Eq. 5 ($2\pi\gamma_r^{-1*}$) or as the imaginary part of the eigenvalue computed with the modified drag coefficient $C'_d = 7.2 \times 10^{-5}$ m s^{-1}($2\pi\gamma_r^{-1**}$)

Particularly, interface displacements of all of nine modes rotates in the clockwise direction; however, the differentiation between Kelvin and Poincaré-type waves is given, depending on the rotation pattern the upper layer flow velocity exhibits: while the upper layer rotates in the clockwise direction for K1 and K2, the upper layer flow velocity rotates in the anti-clockwise direction for the other seven modes shown in Fig. 6c–i.

3.3 Bulk energy dissipation of the Kelvin wave

The modal amplitude of each wave was computed considering the measured wind time series, starting on day 39 of 2009 and finishing on day 52 of 2009. For simplicity, the initial conditions were initially set as zero amplitude (i.e., $\tilde{a}_i = 0$), thereby giving a persistent problem with the phase of the internal waves with respect to the measurements; the simulated waves being faster than those measured (not shown). This aspect is discussed in detail considering the results of the non-linear simulation that are described in the following section.

To include energy dissipation in the linear model, the fitting method proposed by Shimizu & Imberger [28] was conducted, considering as free parameters the damping coefficients, the modal frequencies affected by friction and the initial amplitudes of the first 9 modes. These coefficients were calculated by minimizing the least square error of the simulated temporal evolution of the internal waves with respect to the observed interface displacements, in both TC1 and TC2. The fitted coefficients are shown in Table 2 and final results are shown in Fig. 7a, c, for TC1 and TC2, respectively. Figures 7b, d shows the direct comparison between observed (η_{2obs}) and simulated interface (η_{2sim}) displacements at TC1 and TC2, respectively. The error in the simulations is defined as:

$$error = \sqrt{\frac{1}{n}\sum_{i=1}^{n}(\eta_{2obs} - \eta_{2sim})^2} \tag{7}$$

is shown as dashed lines in Fig. 7b, d and calculated as 0.94 and 0.56 m for TC1 and TC2, respectively.

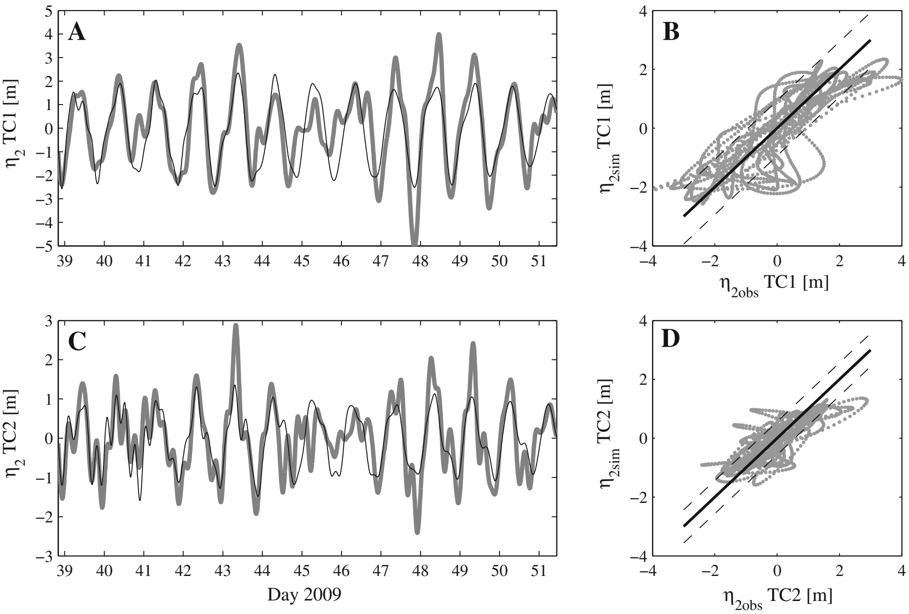

Fig. 7 Linear simulation. **a**, **c** Comparison between simulated (*black thin line*) and measured (*grey thick line*) interface displacements at TC1 and TC2, respectively. **b**, **d** comparison between measured and simulated interface displacements at TC1 and TC2, respectively. *Solid line* denotes perfect fit and *dashed lines* are $\pm error$ defined in Eq. (8).

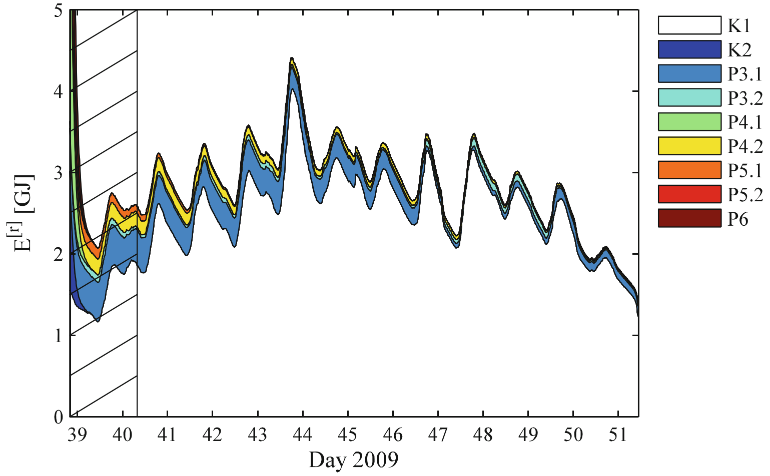

Fig. 8 Simulated modal energy based on the linear solution. *Colors* denote the energy associated to each of the nine modes. *Shaded area* denotes the period of time when the solution is unrealistically influenced by the fitted initial condition

Figure 8 shows the simulated energy partitioning among the 9 modes considered, from which it is observed that the Kelvin wave contains the largest portion of the total energy in the flow, while the energy contained in the other modes was initially high and then it decayed down to about zero energy accordingly to the fitted damping rate. The optimization process fitted high energy on the beginning of the simulations to modes different than K1, and this is due to the influence of the initial condition that minimized the error on early times of the simulation. This period of time, when the solution is unrealistically influenced by the fitted initial condition, is approximately one day and is marked with a shaded region in Fig. 8. Despite of this fitting artifact, it is important to remark that the energy on modes different than K1 monotonically decays according to the fitted damping rate, which revealed that the wind does not provide sufficient energy to waves different than the Kelvin wave. This indicates that further mechanisms are required to explain the observed oscillation in TC2: non-linear interaction between Kelvin and Poincare waves is a reasonable hypothesis as it is shown as follows.

3.4 Non-linear interaction between Kelvin and Poincaré waves

Non-linear interactions among internal waves were computed considering 7 days of measured wind time series, starting on day 39 of 2009. This non-linear simulation required, first, to compute the energy damping coefficient based on the modified drag coefficient $C'_d = C_d\tilde{u} = 7.2 \times 10^{-5}\,\mathrm{m\,s^{-1}}$, with $C_d = 2.5 \times 10^{-3}$ [28] and $\tilde{u} = 2.9\,\mathrm{cm\,s^{-1}}$, where this velocity scale of the lower layer was estimated based on the linear solution. The obtained energy damping coefficients are shown in the last column of Table 2. Based on these damping coefficients and after fitting the initial amplitude of the internal waves, the final results for this non-linear simulation are shown in Fig. 9a, c, for TC1 and TC2, respectively. Figure 9b, d shows the direct comparison between observed (η_{2obs}) and simulated interface (η_{2sim}) displacements at TC1 and TC2, respectively. The error in the simulations was calculated as 1.04 m and 0.56 m for TC1 and TC2, respectively.

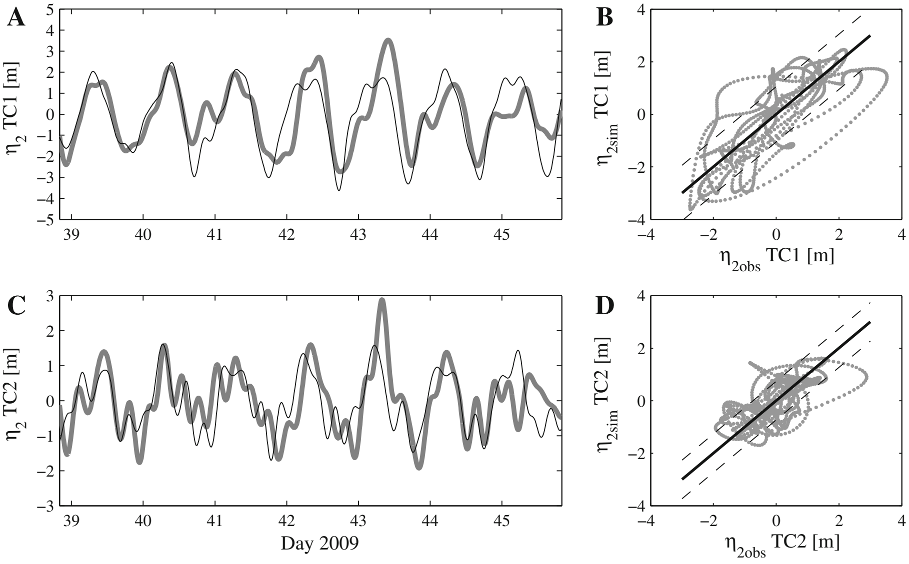

Fig. 9 Non-linear simulation. **a**, **c** Comparison between simulated (*black thin line*) and measured (*grey thick line*) interface displacements at TC1 and TC2, respectively. **b**, **d** comparison between measured and simulated interface displacements at TC1 and TC2, respectively. *Solid line* denotes perfect fit and *dashed lines* are $\pm error$ defined in Eq. (8)

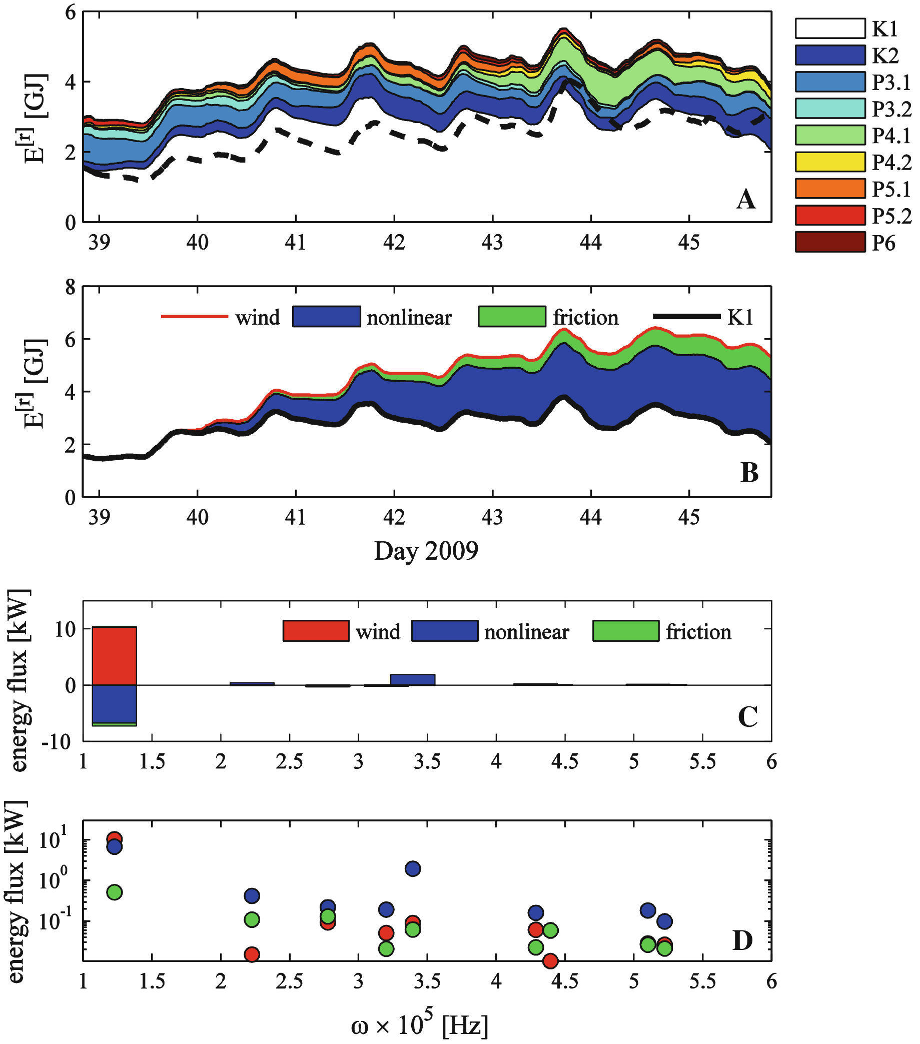

Fig. 10 Non-linear simulation. **a** Simulated modal energy. *Colors* denote the energy associated to each of the nine modes and *dashed line* indicates total energy in K1 simulated with linear model of Fig. 8. **b** Cumulated wind-provided energy (*red line*), cumulated energy dissipated by bottom friction (*green area*), cumulated energy radiated to other modes due to non-linear interaction (*blue area*) and total energy in the Kelvin wave (*black thick line*). **c** Signed energy fluxes related to wind-provided energy (*red*), bottom friction (*green*) and non-linear interaction (*blue*) as function of natural frequency. **d** Absolute value of energy fluxes related to wind-provided energy (*red*), bottom friction (*green*) and non-linear interaction (*blue*), as function of natural frequency in log-scale

Figure 10a shows the simulated energy partitioning among the 9 modes considered, where the dashed line corresponds to the energy on the Kelvin wave simulated with the linear model (Fig. 8a). Once again it is observed that the Kelvin wave contains the largest portion of the total energy in the flow; however, contrary to the linear simulation shown in Fig. 8a, the energy contained in the other modes stayed high during the entire simulation, and in some cases it increases due to non-linear interactions (see orange and green areas, corresponding to mode P5.1 and P4.1, Fig. 6g and e, respectively). The role of non-linear interactions in energy redistribution among basin-scale waves is shown in Fig. 10b–d, where Fig. 10b shows the time series of the energy that enters to the Kelvin wave due to the wind (red line), the cumulated energy in the Kelvin wave that is dissipated by bottom friction (green area), and the cumulated energy that radiates to other modes (blue area). The solid black line corresponds to the simulated energy in the Kelvin wave. Furthermore, Fig. 10c and D shows the temporal average energy fluxes related to the wind input energy (red areas), bottom friction (green areas), and non-linear interaction (blue areas) for each mode. Figure 10c shows signed temporal average of the energy fluxes, being positive if the energy flux increases the energy of the corresponding mode, while Fig. 10d shows the absolute value of the temporal average energy fluxes. The results shown in Fig. 10 are summarized as follows: the Kelvin wave is the dominant wave that is excited by a wind/Kelvin wave resonance, as it is discussed in the following section. After 7 days, approximately 2/3 of this wind-provided energy flux is either radiated to other basin-scale waves or dissipated by bottom friction. Because of non-linear interactions 90 % of this energy flux radiates energy from the Kelvin wave to other basin-scale waves, and only the 10 % is locally dissipated by bottom friction. In this way, the role of non-linear interaction is to distribute the wind-provided energy to other modes, where bottom friction can act to dissipate the total energy in the flow.

The analysis to determine the bulk energy dissipation of the Kelvin wave of Fig. 8 showed that the linear natural period was modified to match with the observations. The simplest explanation for this difference is the fact that non-linearities and friction were neglected in that analysis. To verify this explanation, the phase of the complex amplitude of the Kelvin wave was used to compute the actual angular frequency at which the Kelvin wave rotates (see [31] and [8] for further detail). This computation provided an effective period of the Kelvin wave of 23.24 h, thus explaining the fitted period of the Kelvin 23.3 h.

Figure 5 showed the excitation of a wave with period of about 6 h labelled as point (3), which presents maximum values near the middle of the lake (TC2) rather than in the perimeter (TC1). According to de la Fuente et al. [8] these waves may be related to non-linear interactions between the Kelvin and the Poincaré wave. For the case of Lake Villarrica, non-linear interaction between a fundamental Kelvin wave (with natural period of 22.60 h, Fig. 6a) and the horizontal mode 3 Poincaré-type wave (with natural period of 10.00 h, Fig. 6c) can excite a basin-scale wave with natural period of approximately 6.7 h ($\omega_K + \omega_P$). This triad interaction was observed in the nonlinear simulation, which showed that non-linear interaction energized the basin-scale wave identified as P5.1 (orange area in Fig. 10a), with natural period of 6.47 h (Fig. 6d). Similarly, non-linear interaction between the Kelvin wave and the horizontal mode 2 Kelvin wave (with natural period of 12.57 h, Fig. 6b) can excite a basin-scale wave with natural period of approximately 8.07 h ($\omega_K + \omega_{K2}$), that can be attributed to basin-scale wave identified as P4.1 (green area in Fig. 10a) with a natural period of 8.18 h.

3.5 Wind/Kelvin wave resonance

Numerical simulations and field analysis evidence a resonant dynamics between the Kelvin wave and the periodic wind over the lake, such as that reported by Antenucci and Imberger [2] for Lake Kinneret. Figure 10b plots time series of the energy of the Kelvin wave (thick black line) and the cumulated energy imparted by the wind (red line). The difference between both curves corresponds to the energy dissipated by bottom friction or non-linear energy transfers onto other modes. To further characterize this resonant interaction two analyses were carried out, namely a theoretical solution for modal amplitude equation and an experimental analysis.

3.6 Analytical solution for modal amplitudes equation

Eq. 3 has an analytic solution for constant coefficients and a periodic wind forcing. This solution can be written as:

$$\tilde{a}_r(t) = \omega_r \left[\exp\left(-\gamma_r t\right) \frac{\omega_f \exp\left(i\omega_r t\right)}{\omega_f^2 - \omega_r^2 - 2i\omega_r\gamma_r + \gamma_r^2} - \frac{\exp(i\omega_f t)}{2\left(\omega_f - \omega_r - i\gamma_r\right)} \right. \\ \left. - \frac{\exp\left(-i\omega_f t\right)}{2\left(\omega_f + \omega_r + i\gamma_r\right)} \right] \tag{8}$$

where ω_f denotes the wind frequency, and $\tilde{a}_r(t)$ is written in dimensionless form with respect to the wind magnitude. It is observed that the system reaches a forced equilibrium for $t \rightarrow \infty$, where friction counteracts the wind, thus reaching equilibrium between the resonant wind-given energy and dissipation [2]. Furthermore, in the limit $t \rightarrow \infty$, the oscillating component in Eq. 8 that depends on ω_r vanishes and the flow oscillates in phase with the wind forcing. The amplitude is proportional to $((\omega_f - \omega_r)^2 + \gamma_r^2)^{-1}$. Notice that accordingly to the results presented in Fig. 10, the bulk damping rate γ_r in Eq. 8 should include both bottom friction and non-linear energy radiation to other modes.

3.7 Experimental facilities and results

Motivated by the above field observations and the accompanying analytical modeling study, a set of laboratory experiments was carried out to determine the response to intermittent surface forcing of a two-layer, stably-stratified, rotating fluid within an idealized rectangular box-like container. The experimental facility consisted of a rectangular, bottomless, transparent, acrylic tank with a rigid lid and dimensions 1.840 m long, 0.364 m wide and 0.293 m high. This tank was fixed within a larger rectangular, acrylic container of dimensions 2.140 m long, 0.470 m wide and 0.308 m high, with the (vertical) walls of the inner tank being positioned to leave a small (∼1 mm) gap above the base of the outer tank to permit an endless, taut belt to be traversed horizontally along the base of the tank to simulate the wind shear stress (see Monismith [21]). A geared, externally-mounted, continuously-variable-speed motor controlled the velocity of the belt. The whole system was mounted on a rotating table (see Fig 11) having a prescribed and variable rotation rate. For convenience, the two-layer density stratification inside the tank was established by salinity variations, the magnitudes of which were chosen to satisfy dynamical similarity with the thermally-stratified lake conditions. The stratification was achieved by firstly adding fresh water to the tank until filling to the desired epilimnion height. Saline water of prescribed density was then added very slowly at the base of the tank (to avoid mixing between layers) until the tank was filled completely. In all experiments, the Lake Villarrica aspect ratio $h_1/H = 0.15$ was considered. In order to capture the evolution of the internal waves, four micro-conductivity probes (e.g. Munro and Davies [24]) were mounted on a transverse section (see Fig. 11) at 77 cm from the upwind end and with the sensors at a fixed vertical location 4.5 cm (the prescribed mid-level of the undisturbed pycnocline) from the bottom of the tank. When the filling process was completed, the tank was rotated slowly from rest until the pre-set rotation rate was achieved, in order to minimize interfacial mixing between the two fluid layers. The system was then left for a period of 10–15 h to spin up and achieve solid body rotation [18,37]. All of the forcing experiments with the moving belt commenced after the spin up period had elapsed.

Nine experiments were carried out, forcing the system with a square wave of constant magnitude and period of $T_f = 2\pi\omega_f^{-1}$, generated by turning on the belt during a time equal

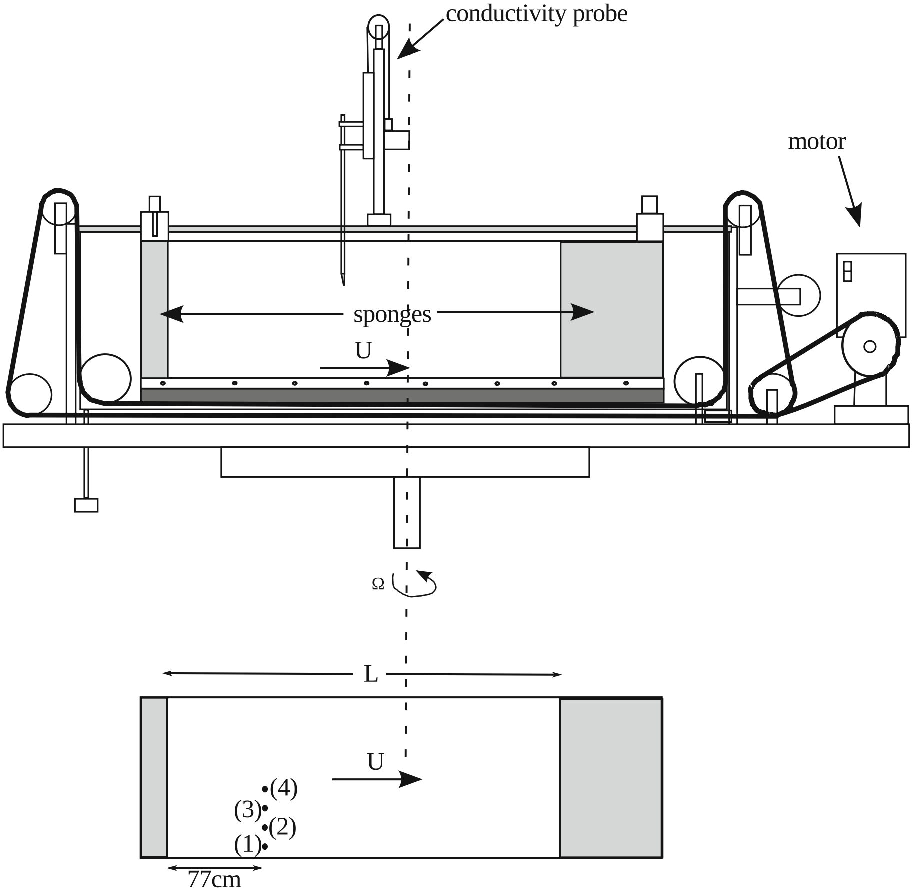

Fig. 11 **a** Side view of main components of the rotating table. **b** Top view and location of the conductivity probes

to 0.5 T_f and then turning off the belt for another 0.5 T_f. The belt speed was kept very low in order to avoid mixing inside the tank. Each run lasted approximately 30 min, with a sampling rate of 15Hz for the micro-conductivity probes. The design parameters of each run are shown in Table 3, and these different runs were defined considering the following criteria: (1) variation of the forcing frequency (runs 1–3, Fig. 12a; 4 and 5, Fig. 12b; 6 and 7, Fig. 12c) to approach the fundamental Kelvin wave frequency, in order to study the influence of the ratio ω_K/ω_f, where ω_K denotes the frequency of the Kelvin wave computed by solving the eigenvalue problem; (2) variation of the angular velocity of the rotating table (runs 2, 4 and 6, Fig. 12d; 3, 5 and 7, Fig. 12e) to study the effect of the ambient rotation for different forcing periods close to the resonant condition; and (3) variation of the stratification (runs 7–9, Fig. 12f) in order to determine the existence of resonance for different periods of the Kelvin wave defined by the density step between layers.

The Wedderburn number is defined here as [15,32]:

$$W = \frac{g' h^2}{u_*^2 L} = \frac{h}{2\eta_o} \tag{9}$$

Table 3 Characteristic parameters of the laboratory experiments

Set	Run	h_1 (cm)	h_2 (cm)	ρ_1 (kg m^{-3})	ρ_2 (kg m^{-3})	W	S	T_K (s)	ω_K/ω_f
1	1	24.8	4.5	999	1,020	156.4	0.47	33.87	0.8
	2	24.8	4.5	999	1,020	156.4	0.47	33.87	0.9
	3	24.8	4.5	999	1,020	156.4	0.47	33.87	1.0
2	4	24.8	4.5	999	1,020	156.4	0.40	34.04	0.9
	5	24.8	4.5	999	1,020	156.4	0.41	34.04	1.0
3	6	24.8	4.5	999	1,020	156.4	0.30	34.42	0.9
	7	24.8	4.5	999	1,020	156.4	0.30	34.42	1.0
4	8	24.8	4.5	999	1,016	160.2	0.30	38.23	1.0
	9	24.8	4.5	999	1,012	160.1	0.30	43.61	1.0

See text for the symbols definition

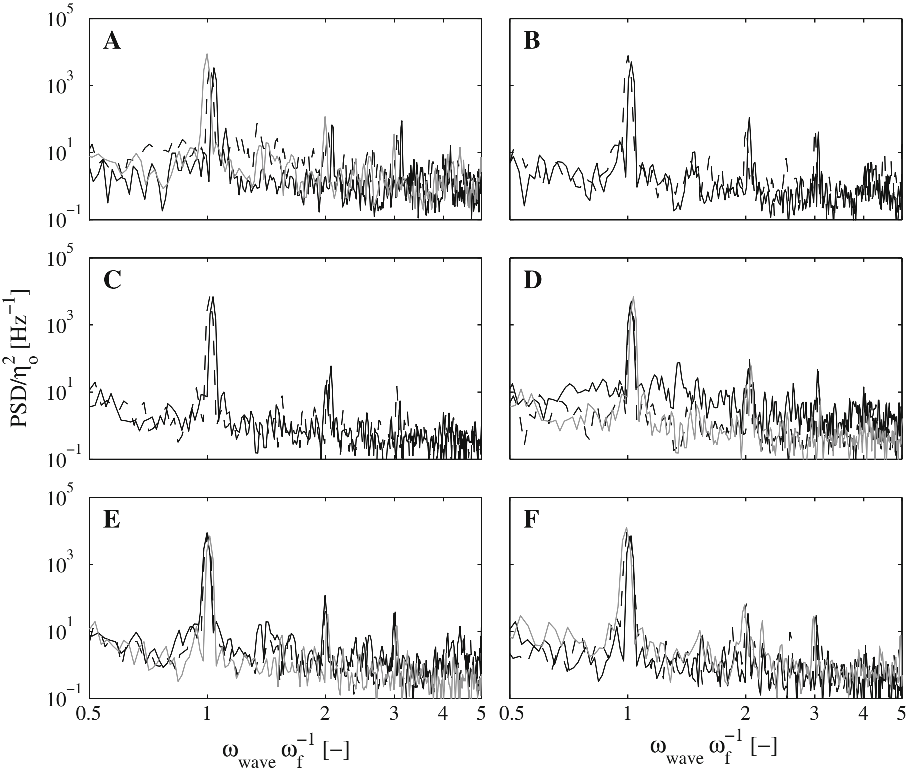

Fig. 12 Average power spectral density normalized by η_o^2 of Eq. 9 versus dimensionless frequency ω/ω_f. **a** Runs 1 (*solid line*), 2 (*dashed black line*), and 3 (*solid grey line*). **b** Runs 4 (*solid line*) and 5 (*dashed black line*). **c** runs 6 (*solid line*) and 7 (*dashed black line*). **d** Runs 2 (*solid line*), 4 (*dashed black line*), and 5 (*solid grey line*). **e** Runs 3 (*solid line*), 5 (*dashed black line*), and 6 (*solid grey line*). **f** Runs 7 (*solid line*), 8 (*dashed black line*), and 9 (*solid grey line*)

where g' is the reduced gravity, h is the epilimnion height equal to h_2 (since the belt is in the bottom of the tank), u_* is the friction velocity of the belt and L is the length of the rectangular basin. Notice that Eq. 9 is equivalent to Eq. 5, as for rectangular basins $L = 2x_g$

(see also Shintani et al. [32]). The Burger number S, originally formulated as a measure of the importance of background rotation for density driven exchange flows in a closed basin [11,36], is defined conventionally here as:

$$S' = \frac{R_0}{B} \tag{10}$$

where $R_0 = c/f$ is the appropriate internal Rossby radius of deformation and B is the transverse width of the rectangular basin (0.364 m).

According to Eq. 8, the forced response of a two-layer system is strongly controlled by the forcing frequency. This is observed in Fig. 12, that shows the average power spectrum that are obtained by group of runs, divided by η_o^2 (Eq. 9) in order to minimize a possible influence on the Wedderburn number, versus the frequency made dimensionless by the forcing frequency. Figure 12 shows that in all the cases, the spectrum has a local maximum around unity, and in multiples of one ($2\omega_f, 3\omega_f$), confirming the behavior predicted by the theory. This is clearer by comparing the dimensionless frequency, f^*, at which the maximum of the spectrum occurs versus the ratio of the Kelvin wave frequency to the wind frequency ω_K/ω_f (Fig. 13a), where it is observed that all of these maximum occur at $\omega_K/\omega_f \approx 1$, although some minor influence of ω_K/ω_f on f^* can be observed; particularly, $f^* = 1.05$

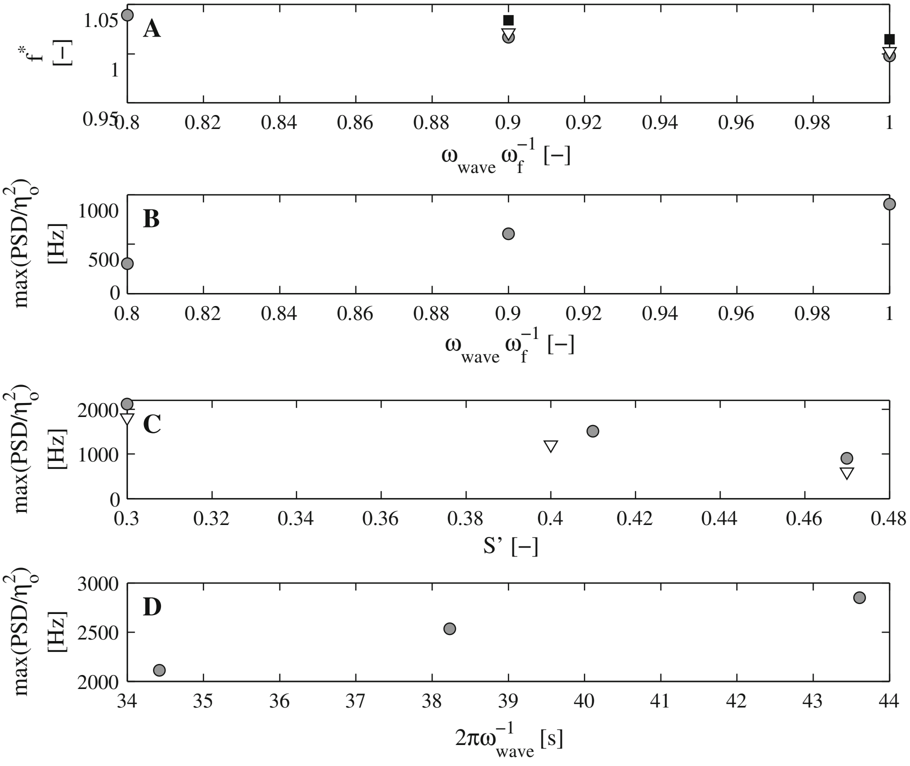

Fig. 13 **a** Dimensionless frequency (ω/ω_f) associated to the maximum in PSD as function of ω_K/ω_f. *Circles* corresponds to set 1, *triangles* to set 2, and *squares* to set 3. **c** Maximum in PSD as function of ω_K/ω_f, using data of set 1. **d** Maximum in PSD as function of S, using data from sets 1 to 3, and *circles* with $\omega_K/\omega_f = 1$ and *triangles* with $\omega_K/\omega_f = 0.9$. **e** Maximum in PSD as function of period of Kelvin wave, using runs 7–9

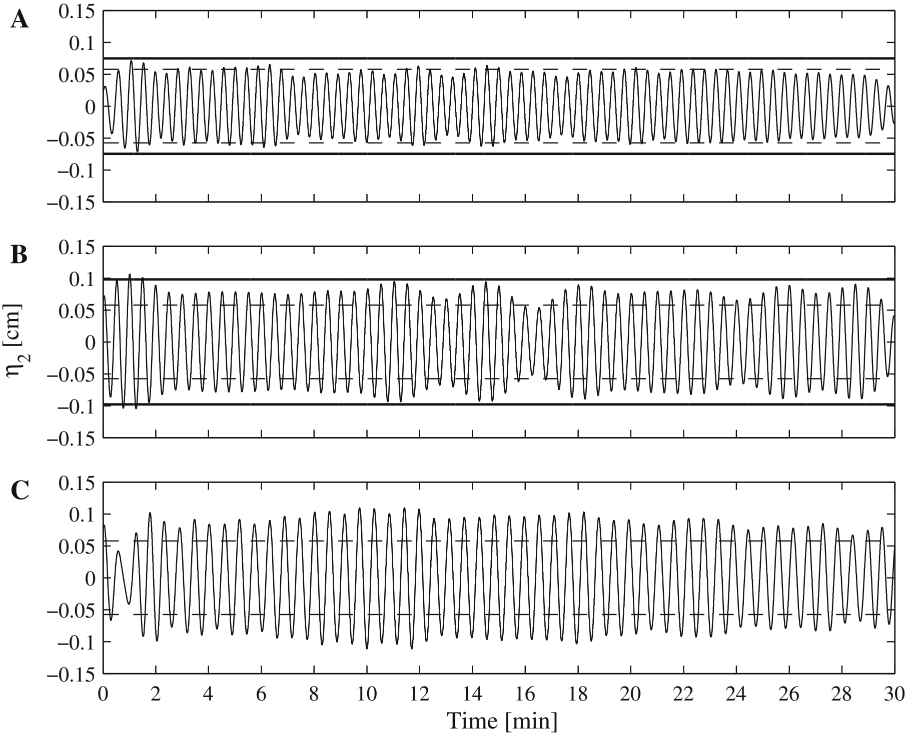

Fig. 14 Interface displacements at probe 2, for experiments **a** 1 ($\omega_K/\omega_f = 0.8$), **b** 2 ($\omega_K/\omega_f = 0.9$) and **c** 3 ($\omega_K/\omega_f = 1.0$). In all three cases W = 156 and S = 0.47. *Horizontal dashed line* defines maximum interface displacements estimated with Eq. 8, and *solid thick line* by correcting this amplitude based on [3]

for $\omega_K/\omega_f = 0.8$, while $f^* = 1$ for $\omega_K/\omega_f = 1.0$. Figure 13b compares the maximum of the PSD as function of ω_K/ω_f, in which it is shown that the spectral maximum increases with ω_K/ω_f with respect to the influence of rotation. Figure 13c compares the maximum of the PSD as function of S', where it is noted that the spectral maximum increases as the Earth's rotation became more important. Finally, with respect to the influence of the period of the Kelvin wave, Fig. 13d compare the maximum in PSD as a function of the period of the Kelvin wave using runs 7–9, where it is observed that there variables are positively related each other, accordingly to Eq. 8.

Finally, Fig. 14 shows the observed interface displacements for three runs (1–3), keeping the Wedderburn and Burger number fixed and varying the forcing frequency to approach the Kelvin wave natural frequency. The amplitude of the oscillation increases as the forcing frequency approaches to the Kelvin wave natural frequency, particularly, the standard deviation of Fig. 14a was 0.039 cm, for Fig. 14b was 0.057 cm, and for Fig. 14c was 0.064 cm; thus confirming the results of Eq. 8 which indicates that the amplitude of a resonant internal wave is controlled by both the magnitude of the forcing described by the Wedderburn number, and the ratio ω_K/ω_f. Boegman and Ivey [3] proposed a relationship to estimate the maximum interface displacements considering the inviscid resonance interaction between the Kelvin wave and the wind (Eqs. 13 and 14 of [3]). This estimation gives that, because of the resonance, internal waves of runs shown in Fig. 14 would be amplified by a factor of 1.3, 1.7 and infinite, respectively. The amplitude of interface displacement expected based on the Wedderburn number (Eq. 8) are shown as a thick dashed line, while the amplitudes estimated considering the resonance are shown with thick black lines. In general, the estimated interface displacements following [3] provide good results for runs 1 and 2, but for run 3 where $\omega_K/\omega_f = 1$. The reason for this inconsistency is on the inviscid assumption of [3]. Eq. 8 shows that damping rates prevent infinite amplitudes when $\omega_K/\omega_f = 1$. The Kelvin wave becomes in resonance when the forcing frequency matches the wave frequency. It is concluded that friction is the damping mechanism that controls the unlimited amplitude growth of the interface oscillations. Mixing, although it is not so important in the laboratory system because the conveyor belt velocity is low, tends to change the Kelvin wave period while the forcing frequency remains constant. Thus, the intensity of the resonance in the system varies.

4 Discussion

Field data have been collected to study the vertical thermal structure of Lake Villarica during the summer of 2009. Numerical modeling was conducted for a two-layer system forced by the Earth's rotation and the wind stress over the lake surface. The results obtained allow the observed displacements of the density interface to be explained, specifically with regard to the resonant excitation of internal waves due to the linear and non-dissipative equations considered in the analysis [31].

The applied linear and non-linear modal analysis gives good results. The obtained modes were used to study the energy dissipation within the system, which is necessary to control the amplitude growth. The stationary state in the Kelvin wave is then achieved when the periodic wind-provided energy is constantly dissipated by bottom friction and radiated to other modes. The results obtained from the optimization process of the linear modal analysis indicated that the dissipation time-scale of the Kelvin wave was 38.1 days; however, the non-linear simulation indicates that only 10 % of this dissipation rate is actually because of bottom friction, while the rest 90 % represents the energy that is radiated from the Kelvin wave to other modes. Figure 10c shows that the energy flux due to non-linear interactions that radiates energy from the Kelvin wave to the other modes is 0.52 GJ day^{-1}, and the energy flux due to bottom friction is 0.04 GJ day^{-1}. This provides a bulk energy flux of 0.56 GJ day^{-1}, which in the context of 2.75 GJ of energy contained in the Kelvin wave, provides a bulk damping time-scale of 31.4 days ($T_{Kelvin} = 2\pi\gamma_{Kelvin}^{-1}$), which matches with the estimated value of 30.2 days with Eq. 5. The steepening formation time, T_s/T_i, characterizes the ratio between the time scale of the steepening of basin-scale waves with respect to the internal seiche time scale [6,15,35] and, for wave amplitudes of about 3 m in Lake Villarrica, this ratio is equal to about 2, indicating that nonlinearities in the flow are not relevant. However, the results shown in this article indicate that weak nonlinearities of the flow are indeed required to explain the energy path that transfers from larger scales to the smallest. This mechanism, together with the effects of bottom friction, explains the bulk dissipation rate estimated here.

An alternative way to estimate the friction energy flux of the entire flow is by considering it equal to $\rho\ C_d\ \tilde{u}^3\ A$ where A is the area of the lake (176 km^2), $\rho = 1{,}000\,\mathrm{kg\,m^{-3}}$, $C_d = 2.5 \times 10^{-3}$ and $\tilde{u} = 2.9\,\mathrm{cm\,s^{-1}}$, where this velocity scale of the lower layer was estimated based on the linear solution. This estimation provides that the total energy flux due to bottom friction is 10.45 kW. This value matches to the wind energy flux to the Kelvin wave (10 kW, Fig. 10). Consequently, there is a long term balance between the wind energy flux that energizes K1, and friction energy flux of the entire flow. Nonlinear interaction between modes is required to redistribute the energy that enters to the Kelvin wave to other modes that contribute to bottom dissipation.

Experimental results confirm the resonant interaction between the horizontal mode 1 Kelvin wave and the wind. These results could be extended in order to quantify the energy cascade between the Kelvin wave and higher-frequency modes, until energy is dissipated by friction and the pycnocline is eroded by turbulent mixing.

The scope of this study was related to the oscillations generated by the basin-scale internal waves in the lake and the interaction of the upper layer velocity field with the spatially-uniform forcing wind blowing over the lake. Characterization of the velocity field, in particular the vertical velocity distribution, could be improved considering 3D models.

In this research a modal analysis technique and experimental analysis were used to explain field measurements in Lake Villarrica. Based on this analysis, a fundamental Kelvin wave was identified, being in a resonant interaction with the daily wind that blows over the lake. Theoretical analysis, numerical simulations and laboratory experimental results confirm resonance. Also, this study shows that modes with periods between 5 and 8 h are excited by non-linear interactions between fundamental Kelvin wave and horizontal Poincaré-type waves.

Acknowledgments The authors acknowledge support of the Civil Engineering Department, Universidad de Chile, FONDECYT Project 1080617 and the Civil Engineering Department, University of Dundee. The first author acknowledges financial support from Department of Graduate and Postgraduate Degree, Universidad de Chile. Finally, the authors would also like to thank to the anonymous reviewers of this article who provided helpful, interesting and constructive comments.

References

1. Antenucci JP, Imberger J (2001) Energetics of long internal gravity waves in large lakes. Limnol Oceanogr 46:1760–1773
2. Antenucci JP, Imberger J (2003) The seasonal evolution of wind/internal wave resonance in Lake Kinneret. Limnol Oceanogr 48:2055–2061
3. Boegman L, Ivey GN (2012) The dynamics of internal wave resonance in periodically forced narrow basins. J Geophys Res 117:C11002. doi:10.1029/2012JC008134
4. Boegman L, Imberger J, Ivey GN, Antenucci JP (2003) High-frequency internal waves in large stratified lakes. Limnol Oceanogr 48:895–919
5. Boegman L, Ivey GN, Imberger J (2005a) The energetics of large-scale internal wave degeneration in lakes. J Fluid Mech 531:159–180
6. Boegman L, Ivey GN, Imberger J (2005b) The degeneration of internal waves in lakes with sloping topography. Limnol Oceanogr 50:1620–1637
7. Cushman-Roisin B (1994) Introduction to geophysical fluid dynamics. Prentice Hall, New York
8. de la Fuente A, Shimizu K, Imberger J, Niño Y (2008) The evolution of internal waves in a rotating, stratified, circular basin and the influence of weakly nonlinear and nonhydrostatic accelerations. Limnol Oceanogr 53(6):2738–2748
9. de la Fuente A, Shimizu K, Niño Y, Imberger J (2010) Nonlinear and weakly nonhydrostatic inviscid evolution of internal gravitational basin-scale waves in a large, deep lake: Lake Constance. J Geophys Res 115:C12045. doi:10.1029/2009JC005839
10. Fischer H, List E, Koh R, Imberger J, Brooks N (1979) Mixing in inland and coastal waters. Academic Press, New York
11. Garvine RW (1987) Estuary plumes and fronts in shelf waters: a layer model. J Phys Oceanogr 11:1877–1895
12. Gill AE (1982) Atmosphere–ocean dynamics. Academic Press, London
13. Helfrich K, Melville W (2006) Long nonlinear internal waves. Annu Rev Fluid Mech 38:395–425
14. Hodges BR, Imberger J, Saggio A, Winters KB (2000) Modeling basin-scale internal waves in a stratified lake. Limnol Oceanogr 45:1603–1620

15. Horn D, Imberger J, Ivey GN (2001) The degradation of long-scale interfacial gravity waves in lakes. J Fluid Mech 434:181–207
16. Imberger J (1998) Flux paths in a stratified lake: a review. In Imberger J (ed) Physical processes in lakes and oceans, coastal and estuarine studies, vol 54. American Geophysical Union, Washington, pp 1–17
17. Imberger J, Hamblin PF (1982) Dynamics of lakes, reservoirs and cooling ponds. Annu Rev Fluid Mech 14:153–187
18. Linden PF, van Heijst GJF (1984) Two-layer spin-up and frontogenesis. J Fluid Mech 143:69–94
19. Meruane C, Niño Y, Garreaud R (2005) Simulation of phytoplankton response to strong wind events in Lake Villarrica, Chile. In: Proceedings of the XXXI IAHR congress. Seoul, Korea
20. Miles JW (1984) Resonantly forced surface waves in a circular cylinder. J Fluid Mech 149:15–31
21. Monismith SG (1986) An experimental study of the upwelling response of stratified reservoirs to surface shear stress. J Fluid Mech 171:407–439
22. Mortimer CH (1974) Lake hydrodynamics. Mitt Int Ver Limnol 20:124–197
23. Münnich M, Wüest A, Imboden DM (1992) Observations of the second vertical mode of the internal seiche in an alpine lake. Limnol Oceanogr 37:1705–1719
24. Munro RJ, Davies PA (2006) The flow generated in a continuously stratified rotating fluid by the differential rotation of a plane horizontal disc. Fluid Dyn Res 38:522–538
25. Nurser AJG, Lee M-M (2004) Isopycnal averaging at constant height. Part I: the formulation and a case study. J Phys Oceanogr 34:2721–2739
26. Preusse M, Peeters F, Lorke A (2010) Internal waves and the generation of turbulence in the thermocline of a large lake. Limnol Oceanogr 55(2010):2353–2365
27. Saggio A, Imberger J (1998) Internal wave weather in a stratified lake. Limnol Oceanogr 43:1780–1795
28. Shimizu K, Imberger J (2008) Energetics and damping of basin-scale waves in a strongly stratified lake. Limnol Oceanogr 53:1574–1588
29. Shimizu K, Imberger J (2009) Damping mechanisms of internal waves in continuously stratified rotating basins. J Fluid Mech 637:137–172
30. Shimizu K, Imberger J (2010) Seasonal differences in the evolution of damped basin-scale waves in a shallow stratified lake. Limnol Oceanogr 55(3):1449–1462
31. Shimizu K, Imberger J, Kumagai M (2007) Horizontal structure and excitation of primary motions in a strongly stratified lake. Limnol Oceanogr 52:2641–2655
32. Shintani T, de la Fuente A, Niño Y, Imberger J (2010) Generalizations of the Wedderburn number: parameterizing upwelling in stratified lakes. Limnol Oceanogr 55(3):1377–1389
33. Thompson R, Imberger J (1980) Response of a numerical model of a stratified lake to wind stress. In: Proceedings of 2nd international symposium on stratified flows, vol 2, pp 562–570, Trondheim, Norway
34. Thorpe SA (1974) Near-resonant forcing in a shallow two-layer fluid: a model for the internal surge in Loch Ness. J Fluid Mech 63:509–527
35. Ulloa H, de la Fuente A, Niño Y, Rozas C, García CM (2011) Experimental study of the free evolution of the internal gravitational waves affected by Coriolis in a stratified flow. In: 7th international symposium on stratified flows, Rome, Italy
36. Valle-Levinson A (2008) Density-driven exchange flow in terms of the Kelvin and Ekman numbers. J Geophys Res 113:C04001
37. Van Heijst GJF, Davies PA, Davis RG (1990) Spin-up in a rectangular container. Phys Fluids A 2(2):150–159
38. Wake GW, Hopfinger EJ, Ivey GN (2007) Experimental study on resonantly forced interfacial waves in a stratified circular cylindrical basin. J Fluid Mech 582:203–222
39. Wang Y, Hutter K, Baüerle E (2000) Wind-induced baroclinic response of Lake Constance. Ann Geophys 18:1488–1501
40. Wüest A, Lorke A (2003) Small-scale hydrodynamics in lakes. Annu Rev Fluid Mech 35:373–412